Journal of Wind Engineering & Industrial Aerodynamics 209 (2021) 104485

Contents lists available at ScienceDirect

Journal of Wind Engineering & Industrial Aerodynamics

journal homepage: www.elsevier.com/locate/jweia

A comparison of lab-scale free rotating wind turbines and actuator disks

Sanne de Jong Helvig [a], Magnus K. Vinnes [a], Antonio Segalini [b], Nicholas A. Worth [a], R. Jason Hearst [a,*]

[a] Department of Energy & Process Engineering, Norwegian University of Science & Technology, NO-7491, Trondheim, Norway
[b] Linné Flow Centre, STandUP for Wind, KTH Mechanics, Stockholm, Sweden

ARTICLE INFO

Keywords:
Wind turbine
Actuator disk
Lab-scale
POD

ABSTRACT

Planar particle image velocimetry was conducted upstream and in the near-wake of a lab-scale free-rotating wind turbine model and compared to several actuator disks with the same dimensions. The Reynolds number of the incoming flow is order 10^4. Actuator disks with different designs and solidities were tested, and the process of actuator disk selection is explicitly shown. The drag, mean velocity and mean vorticity in the wake of the disks were compared to that of the rotating model. For the disk that was the best match, the Reynolds stresses and swirling strength are also presented. The instantaneous swirling strength illustrated that despite similar mean fields, the instantaneous phenomena were significantly different. Distinct tip vortices were present in the wake of the rotating model but were absent from the wake of the actuator disk. Proper orthogonal decomposition was used to further investigate the underlying phenomena in the two flows, again demonstrating the importance of tip vortices when studying the rotating model and the lack of such distinct vortices when using the actuator disk. Hence, despite well-matched mean characteristics, the instantaneous structures in the two flows remain distinct.

1. Introduction

Renewable energy now accounts for a third of global power capacity, and, according to Siemens (2019), wind power alone may represent one third of the global electric demand by 2040. Placing wind turbines in wind farms is the most economic and efficient implementation with respect to planning, maintenance and use of land and infrastructure. However, it means that the turbines are permanently exposed to the wakes caused by upstream rows of turbines, and hence, Veers et al. (2019) stated that the first grand challenge in wind energy research today is to improve the understanding of wind farm flow physics. Porté-Agel et al. (2019) also described the importance of further developing models for wind farm wake flow studies and extending these studies to include factors such as topography, thermal stability and the role of atmospheric turbulence. Moreover, in their 'future perspectives', Porté-Agel et al. (2019) emphasised the need for continued wind tunnel testing "to provide further physical insight on the flow, and to guide the improvement, calibration and validation of […] numerical models".

Field tests of wind farms have been, and continue to be, carried out (Barthelmie and Jensen, 2010; Smith et al., 2013; Barthelmie et al., 2015; Zhan et al., 2019, 2020), but such approaches are expensive, difficult and, by their nature, incapable of being completely controlled, unlike lab-scale experiments. Using small-scale models makes it possible to study wind farms in a wind tunnel. Lab-scale experiments are thus helpful in providing a deeper understanding of large scale physics at a range of different conditions, e.g., different incoming flow velocities and turbulence levels (Hearst and Ganapathisubramani, 2017; Li et al., 2020). Multiple small-scale wind farm experiments have already been performed (Theunissen et al., 2015; Camp and Cal, 2016, 2019; Bossuyt et al., 2017; Segalini and Dahlberg, 2020), providing new knowledge of wind farm flows and how to improve wind farm efficiency (Stevens and Meneveau, 2017). However, the complexity of constructing and using numerous rotating turbine models is challenging, which is why, on occasion, simplifications are sought.

The actuator disk is a common simplification of a rotating blade, horizontal-axis wind turbine, used both in experiments and simulations. The simple structure of a static actuator disk is easier to simulate than the blades of a moving rotor, allowing for fewer grid cells, which can have larger dimensions, and hence allowing for larger time steps. In turn, the simulations are not as computationally intensive. Stevens and Meneveau (2014) used actuator disks in simulations to study the effect of wind-input variability on wind farm power fluctuations. Later, Stevens et al. (2014) used actuator disks when simulating and studying row alignment in wind farms. Wu and Porté-Agel (2012) used actuator disk

* Corresponding author.
E-mail address: jason.hearst@ntnu.no (R.J. Hearst).

https://doi.org/10.1016/j.jweia.2020.104485
Received 15 June 2020; Received in revised form 13 November 2020; Accepted 4 December 2020
Available online xxxx

simulations to study atmospheric turbulence effects on wind turbine wakes. Work has been done on testing and further developing the actuator disk as a simulation tool, and comparing the simulations to experimental results (Harrison et al., 2010; Wu and Porté-Agel, 2011; Martínez Tossas et al., 2014; Lignarolo et al., 2016a; Simisiroglou et al., 2017). Static actuator disks are also easier and less costly to manufacture en masse for use in experiments, and often more robust than using moving parts. Blackmore et al. (2013) used actuator disks as a simplification for tidal turbines to study the effect of turbulence on drag force in a water current. Howland et al. (2016) examined the deflection and morphology of wakes behind an actuator disk model of a wind turbine operating in yawed conditions. Bossuyt et al. (2017) used actuator disks to model different wind farm layouts to examine unsteady loading. Theunissen et al. (2015) conducted actuator disk wind farm experiments as a validation, and possible source of improvement, of the actuator disk as a computational tool. While the actuator disk is shown to be a common and convenient simplification, how well actuator disks replicate the behavior of rotating turbines, and how much of an influence the actuator disk geometry has, is still being established.

Actuator disks are typically designed to resemble a specific rotating wind turbine, by matching the diameter of the disk with the diameter of the rotor, and by matching the drag coefficient (sometimes referred to as the "thrust coefficient" in wind turbine literature). Besides that, there are to date no standards in terms of actuator disk design and production. Camp and Cal (2016, 2019), Bossuyt et al. (2017) and Neunaber (2018) used designs with a solidity that decreases with radial coordinate. Aubrun et al. (2013), and later Lignarolo et al. (2014, 2016b), used fine metal meshes with varying porosity at the center of the disk and the outer edge. Blackmore et al. (2013) used a pattern of circular, equally sized holes to maintain approximately uniform porosity across the radius. Sforza et al. (1981) made their actuator disks from perforated metal plates, while Pierella and Sætran (2010) used wooden grids, and Myers and Bahaj (2010) used thin sheets of PVC plastic to create mesh disks. Different actuator disk designs are essentially used interchangeably. Aubrun et al. (2019) conducted a round-robin test of actuator disks, comparing a mesh disk to a non-uniform disk with radially decreasing solidity. They showed that the disks are not overly comparable, and that the variation across facilities is quite large. Theunissen and Worboys (2018) examined the effect of hole topology on the produced drag and near-wake characteristics of actuator disks. With the exception of Aubrun et al. (2019) and Theunissen and Worboys (2018), few comparisons between the different disk design layouts have been conducted, and when actuator disks are used in experiments, the process of actuator disk selection is rarely explicit. The employed disk is simply said to have a certain design, and to match the two previously mentioned criteria of disk diameter and produced drag. Developing a standard actuator disk design which produces the desired wake would be both efficient and practical in order to create uniformity and comparability between experiments. In order to do so, however, more knowledge on the flow field behind actuator disks is needed, which is the focus herein.

After creating an actuator disk that matches the diameter and the produced drag, previous studies have examined the similarity of the flow field behind the actuator disk and the rotating model. The main question has been whether the wake can be properly modeled in the absence of the rotational momentum induced by rotating blades (Neunaber, 2018). Aubrun et al. (2013) used hot-wire measurements, and found that the wake of a rotating model and their porous disk in a modeled atmospheric boundary layer were indistinguishable at 3D downstream. A comparison at low turbulence inflow was also acceptable. Lignarolo et al. (2016b) conducted Particle Image Velocimetry (PIV) measurements in the wakes of both models. They showed that by matching the diameter and drag coefficient, the energy coefficient, velocity, pressure, enthalpy field and wake expansion matched, even in the absence of inflow turbulence. However, differences were found in terms of turbulence intensity and turbulent mixing within their field of view, stretching to 2.18D downstream, due to the presence of tip vortices behind the rotating model. They concluded that the wakes are in good agreement, and suggested the possibility to extend the use of the actuator disk model into the very near wake, given that turbulent mixing is correctly represented. Camp and Cal (2016) found that the mean kinetic energy transport in the far wake is adequately represented by the actuator disk, however in the near wake, significant discrepancies exist in the areas where rotation is a key phenomenon. Additionally, the main difference in the mean velocity in the near wake was the out-of-plane component, resulting from the rotation of the rotor, whereas the mean velocity is nearly the same in regions where rotation is not a critical phenomenon. They do, however, conclude that the results are encouraging for modelers who employ the actuator disk model for simulations of wind farms. Hence, there is a general agreement that the actuator disk is an adequate simplification in the far wake, and that there are certain discrepancies in the near wake, especially in the areas that are strongly affected by rotation when using a rotating model. It is important to note that the compared characteristics are usually mean flow characteristics. Despite a similarity of the mean flows, the instantaneous phenomena in the two wakes might still differ. Current literature examining the instantaneous flows and the fundamental structures constituting the flows is sparse. Camp and Cal (2019) compared a three-bladed rotating turbine model with an actuator disk using PIV. They applied snapshot Proper Orthogonal Decomposition (POD) and examined the invariants of the Reynolds stress anisotropy tensor, discovering discrepancies in the underlying spatial structures and the anisotropic character of the two wakes. While Camp and Cal (2019) have started to explore the issues of structural comparability of the wakes of actuator disks and rotating models, more research is needed to better understand the differences. By gaining more knowledge on how to improve the actuator disk model, it can become an accurate and simple tool for the industry.

The aim of this work is to examine how comparable a well matched actuator disk is to a rotating turbine instantaneously. The process of actuator disk selection is shown in detail, in order to determine how different disk designs and solidities affect the flow field. All actuator disks designed for the selection process are based on designs used in the literature. The results are therefore important to improve the knowledge of the flow physics in wakes of small-scale wind turbine models already used for research. For all the studied flow characteristics, the full streamwise 2D plane up to $x/D = 3.3$ is examined. This differs from the work of Aubrun et al. (2013) and Lignarolo et al. (2016b) who studied smaller fields of view, and Camp and Cal (2019) who conducted their POD analysis within limited sections of the downstream direction of their field of view. Further, the actuator disk whose wake most resembles the wake of the rotating model based on mean flow characteristics is chosen. The instantaneous phenomena and spatial structures in the wake of this actuator disk are examined and compared to the wake of the rotating model, in order to determine the potential similarities and differences of the underlying flow structures.

2. Experimental method

2.1. Facility

The experiments were conducted in the small closed-loop wind tunnel in Strømningslaben at NTNU; the test section measures 1 m × 0.5 m × 7 m (width × height × length). The present study was conducted 3 m downstream of the wind tunnel contraction. The inflow is uniform, with a maximum velocity of 35 m/s and a background turbulence intensity of 0.7%. It is the same facility as used by Skeide et al. (2020).

2.2. Test cases

Small-scale models were used in this study to examine the characteristics of models that are relevant for wind farm experiments, as mentioned in the introduction. The used rotating wind turbine models, hereafter referred to as the rotating models (RM), have two-bladed

plastic rotors connected to a sliding bearing. Magnets are placed at the bottom of the tower to facilitate the mounting. They have a rotor diameter of $D = 45$ mm and a hub height of 65 mm. The tip-speed-ratio ($TSR = \Omega D/2U_h$, where Ω is the angular velocity of the blade tip and U_h is the velocity at hub height) of the freely rotating models is approximately 4.8. This is slightly lower than, but still on the same order of magnitude as, utility scale turbines, which usually operate at $TSR \approx 6 - 8$. The maximum chord Reynolds number is on the order of $Re_c = U_r c/\nu = 2 \times 10^4$. Here, U_r is the local velocity experienced by the airfoil at a certain radius and c is the chord length. At low Reynolds numbers, thin airfoils have been shown to perform better than conventional airfoils (Sunada et al., 1997). Thus, the rotor blades are cambered plates with a thickness of 0.5 mm. The maximum chord length is $c = 8$ mm. The same models were used by Ebenhoch et al. (2017) and Segalini and Dahlberg (2020), and the RMs are thus representative of models used in lab-scale wind farm experiments.

The actuator disks were designed using SolidWorks and then 3D printed using an Ultimaker 2+ with PLA. Using computer-aided design (CAD) and 3D printing implies that the disk designs can easily be shared and reproduced; the CAD files of the geometries can be found in the Supplementary Material of this work. The disks were designed with a diameter of 45 mm to match the rotating turbine, and a thickness of 2.5 mm. Two different actuator disk designs were tested. The first has uniform circular holes and is intended to be similar in style to the mesh actuator disks used by Aubrun et al. (2013) and Lignarolo et al. (2016b). Hereafter, the disks with this design are referred to as Uniform Holes Disks (UHD). The second design has trapezoidal holes that increase in size as the radial coordinate increases, similar to the design employed by Camp and Cal (2016, 2019) and Bossuyt et al. (2017). The solidity of these disks decrease with radial coordinate, matching a characteristic of an actual wind turbine. Disks with this design are referred to as Nonuniform Holes Disks (NHD).

Three different solidities were tested: 35%, 40% and 60%. The disks are named UHD and NHD followed by the number describing their solidity, e.g., NHD35 for the 35% solidity disk with the NHD design. Due to limitations in the 3D printing process, producing 35% solidity with the UHD design proved problematic without letting the holes influence the perimeter of the disk. Hence, a 35% solidity disk with the UHD design is not included in the current work. A solid disk was also made for reference. All the disks can be seen in Fig. 1.

The actuator disks were designed with a small hole in the center in order to connect them to towers. This design resulted in a large solidity in the center of the disks, which can represent the nacelle of a wind turbine (Neunaber, 2018). The tower was designed to match the RM's tower, and a magnet was placed at the bottom of it.

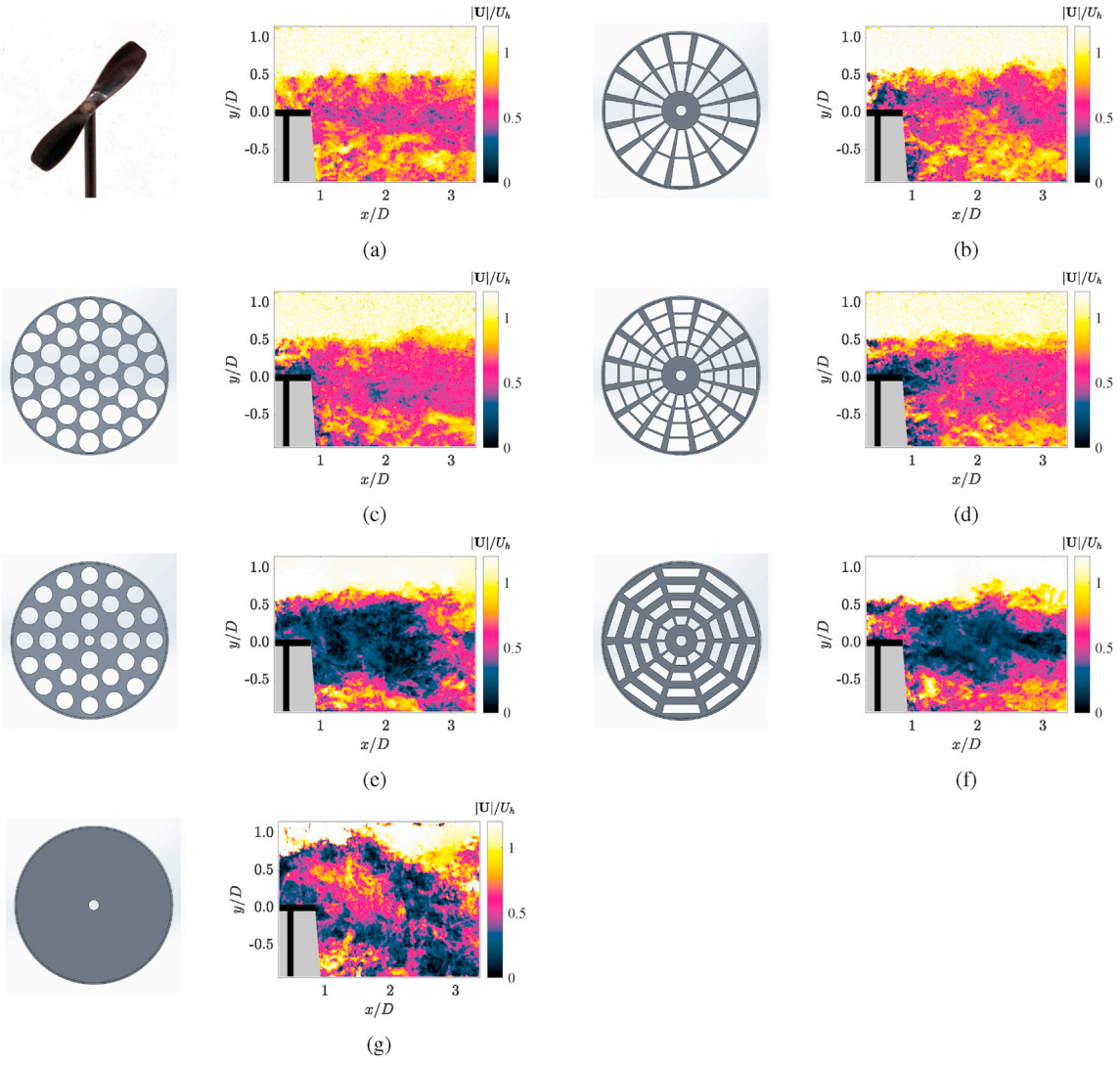

Fig. 1. All actuator disk designs and a picture of the RM, next to an image of the instantaneous total velocity field behind the respective disk and the RM. (a) RM, (b) NHD35, (c) UHD40, (d) NHD40, (e) UHD60, (f) NHD60 and (g) the solid disk.

2.3. Force measurements

Underneath the wind tunnel is a six-component AMTI BP40060HF 1000 force plate, able to measure the force and moment components along the x-, y- and z-axes. Here, x is the downstream, longitudinal direction, y is upwards, and z completes a right-hand system.

A test rig was constructed to measure the forces, consisting of a 0.5 m long magnetic steel bar that stretched along the width of the wind tunnel, on top of an aluminium cylinder that passed through a small hole in the floor of the tunnel. The cylinder was then attached to the force plate underneath the tunnel. The steel bar was lifted about 1 cm above the floor of the wind tunnel, to avoid any contact with the floor that could affect the force measurements, and to place the turbine in a uniform stream uninfluenced by the boundary layer developing on the wind tunnel floor. A sketch of the setup, as well as the defined axes and origin, is shown in Fig. 2.

Three models were placed on the test rig while conducting the drag measurements. This was done to ensure that the drag would be within the load cell range and the small changes in solidity would be measurable. Using three models also averages any small differences that might be present between the models. One model was placed in the center of the steel bar, at $z = 0$, and the other two were placed at a distance of $5D$ from it, i.e., at $z = \pm 5D$. The measured drag coefficient,

$$C_D = \frac{F_D}{\frac{1}{2}\rho U_h^2 A}, \tag{1}$$

where F_D is $\frac{1}{3}$ of the measured drag (because three models were used), and $A = \pi D^2/4$ is the reference area, for the RM in the present study is within $\pm 1\%$ of the C_D reported by Ebenhoch et al. (2017) who used the same turbines. This confirms that the setup is appropriate for this measurement.

The drag force in the x-direction was then measured for five different incoming wind velocities, corresponding to five different incoming Reynolds numbers $Re_D = U_h D/\nu$, where ν is the kinematic viscosity of air based on the measured temperature in the wind tunnel. Drag measurements were also conducted having only the test rig and three towers inside the wind tunnel. Each measurement lasted 60 s with a sampling rate of 1000 Hz. Zero measurements were conducted before and after every measurement, to account for potential drift of the force plate. Measurement noise related to the transducer and the electrical equipment gave rise to some uncertainty. Nevertheless, the signal-to-noise ratio improved with the magnitude of the drag force. The lowest Reynolds number shown in the results was selected based on where the signal-to-noise ratio of the system became acceptable. For the Reynolds numbers presented, the uncertainty in the force measurements ranged

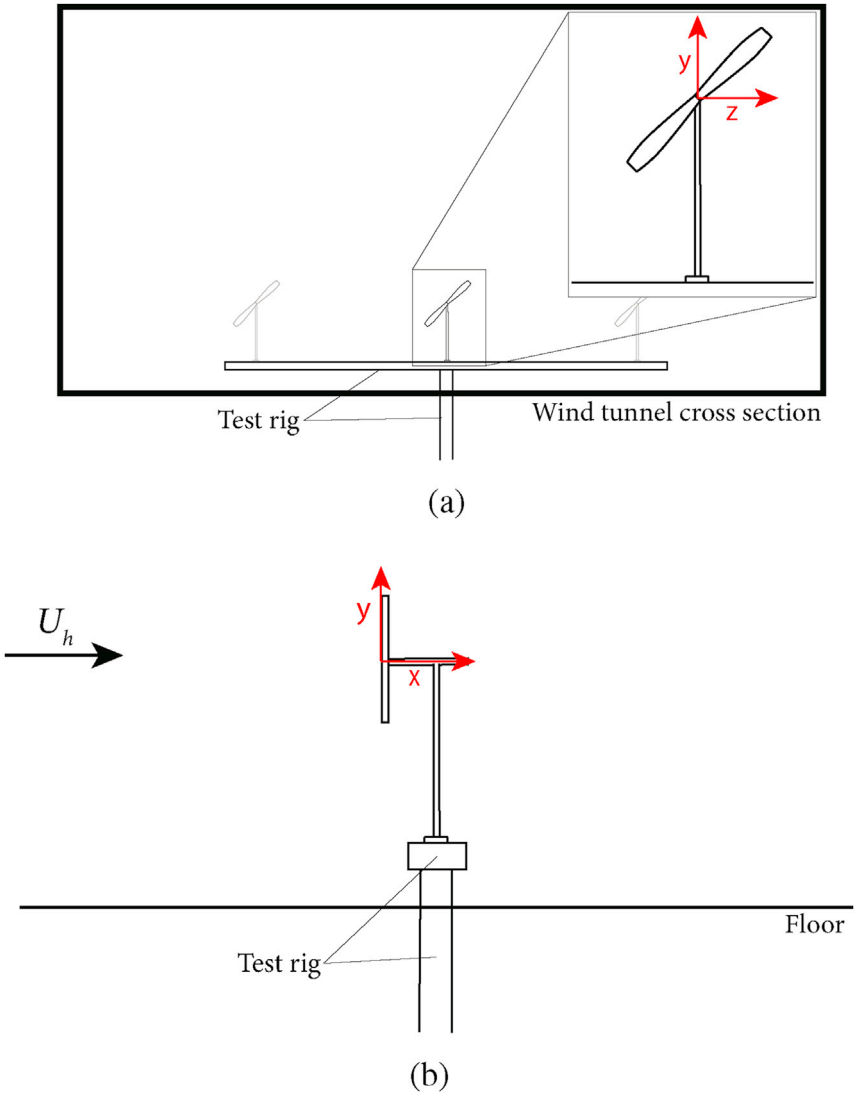

Fig. 2. Sketch of the RMs on the test rig, with the defined axes, (a) from the point of view of the incoming flow and (b) from the side. The grey models were not installed during the PIV acquisition. The sketch is illustrative and not to scale.

from 0.9% to 4%.

2.4. Particle image velocimetry

For the PIV measurements, two LaVision Imager LX 16 megapixel cameras were used, combined with Sigma 180 mm 1:3.5D APO DG Macro lenses. The cameras were mounted outside of the wind tunnel, next to an acrylic window. The first and the second camera had their field of view just upstream and downstream of the turbine rotor, respectively, meaning that the two did not overlap. The first field of view had a range of $-3.01 \leq x/D \leq 0.01$ and $-1.12 \leq y/D \leq 0.92$, while the second had a range of $0.31 \leq x/D \leq 3.33$ and $-0.91 \leq y/D \leq 1.13$. Thus, the near-wake was captured by the second field of view, while the first field of view could be used to quantify the incoming velocity at hub height and to study the characteristics of the incoming flow. In some of the presented results, the data near the upper and lower edge of the field of view have been cropped due to noise arising from particles entering and exiting the domain.

A Litron Nano L200-15 laser, which is a Nd-YAG dual-pulse laser with a measured power of 208 mJ per pulse, was used to illuminate the particles. The laser sheet entered the wind tunnel through an acrylic window in the roof. The particles were seeded using a Martin Magnum 2500 Hz smoke machine and the Martin Rush & Thrill Haze Fluid, producing particles that are approximately 1 μm in diameter. A LaVision PTU X programmable timing unit was used to trigger and synchronize the laser and the cameras. In each measurement, 1000 frames were acquired by each camera. Further acquisition details are provided in Table 1.

The recordings were acquired and processed using LaVision Davis 8.4. Background noise was subtracted from the images by subtracting the minimum value of every pixel over the entire data set, and then over a filter length of 29 image pairs to remove local variations in laser light intensity. Then, the local mean background intensity was filtered out by subtracting the sliding minimum over 20 pixels. The sliding average was calculated over five pixels using a Gaussian profile. Image correction was applied to correct for orthogonality. The processing was then performed with a window size of 96 × 96 pixels and an overlap of 50% for the first pass, while the final window size was 32 × 32 pixels with an overlap of 50%. The resulting uncropped vector field consisted of 307 × 207 vectors.

The 1000 vector fields for each case are independent, and the second-order statistics are converged to within ±8.7% based on the 95% confidence interval. In order to substantially improve this, an order of magnitude increase in the number of samples is required (Cardesa et al., 2012), which is untenable here because of the number of test cases. The uncertainty in the velocity measurement based on the PIV correlation statistics is 2.7% in the high shear, tip-vortex shedding region of the flow where there is high out-of-plane particle movement. This was estimated directly in DaVis using established techniques (Wieneke, 2015; Neal et al., 2015; Sciacchitano et al., 2015). In the rest of the field, the velocity uncertainty is nearer 1.5%.

2.5. Notation

The following notation is used when discussing the results. Each instantaneous velocity, corresponding to one location in one PIV frame, is denoted as $u = u + u'$ and $v = v + v'$ for the velocity in the $x-$ and $y-$directions, respectively, where u' and v' corresponds to the fluctuating parts of the velocity, and u and v are the mean velocities calculated by taking the mean over all 1000 statistically independent PIV measurements. The mean total velocity is $\mathbf{U} = [u, v]$. The measurements are conducted in a 2D plane, and hence the out-of-plane velocity component w is not incorporated into the present analysis. Each characteristic calculated by taking the average over all the PIV measurements is denoted with an overbar.

Table 1
PIV parameters used in data acquisition and processing.

Parameter	Value	Unit
Interframe time	50	μs
Acquisition rate	0.86	Hz
Number of samples	1000	
Field of view ($x \times y$)	3.02 × 2.04	D
Final window size	32 × 32	pixels
Window overlap	50	%
Vectors ($x \times y$)	307 × 207	

3. Drag measurements

Since actuator disks are usually designed to match the drag of a rotating turbine, the first step was to conduct drag measurements. For each model and at each incoming Reynolds number, the average drag force over the 60 s measurement was calculated, and the drag resulting from the test rig and the towers was subtracted. As three models were used during the drag measurements, the drag force was then divided by three, arriving at the drag acting on only one disk or one set of rotating blades. The drag coefficient as a function of Reynolds number is plotted in Fig. 3 for all the models.

Lignarolo et al. (2016b) showed drag coefficients as a function of actuator disk solidity based on the results presented in six different papers, and concluded that the drag coefficient decreases approximately linearly with decreasing solidity. That is also the case for the current measurements. As expected, the solid disk produces a much higher drag coefficient than the RM. The drag coefficient of the solid disk at $Re_D = 3 \times 10^4$ is omitted from the figure, as it deviates from the others by more than 42 standard deviations, and is thus regarded as an outlier.

The drag coefficients seem to concentrate around some mean value, suggesting that the non-dimensional drag is Reynolds number independent over the presented Re range. The average drag coefficient over the different Reynolds numbers was calculated, along with the standard deviation, and is presented in Table 2 for the RM and the actuator disks with 35% and 40% solidity. The NHD35 is the best match compared to the drag coefficient of the RM, with a deviation of 1.8%.

4. Reynolds number dependence of the velocity field

For the RM and NHD35, PIV measurements were conducted at five different incoming Reynolds numbers, relating to five different incoming flow velocities at hub height, U_h. This was done to check whether the normalized velocity in the wake would vary as a function of the incoming Reynolds number, since the non-dimensional drag was Reynolds number independent in this regime. The mean velocity field was calculated and then normalized by U_h. The streamwise velocity component is the dominant component of the total velocity. Hence, Fig. 4 depicts the streamwise velocity component at five downstream locations for all five incoming Reynolds numbers for the RM and the NHD35. The first profile is from shortly behind the end of the model tower, and the last profile is located close to the end of the field of view.

For the actuator disk, the normalized velocity profiles overlap at all the downstream locations. On average, the standard deviation between the measurements as a percentage of the mean value is 2.4% in the entire field of view. Thus, the actuator disks are independent of Reynolds number within the investigated range.

For the RM, the lines illustrating the normalized streamwise velocity generally follow the same pattern and largely overlap as close to the disk as 1D downstream. By 3D downstream, the velocity profiles are in very good agreement. However, it can be seen that the two lowest Reynolds numbers produce a slightly different profile at 1D, e.g., behind the nacelle at $y/D = 0$, implying that the RM's wake is only Reynolds number independent above some threshold Reynolds number. Studying the three highest Reynolds numbers, starting at $Re_D = 3 \times 10^4$, an average standard deviation of 3.3% of the mean value is found.

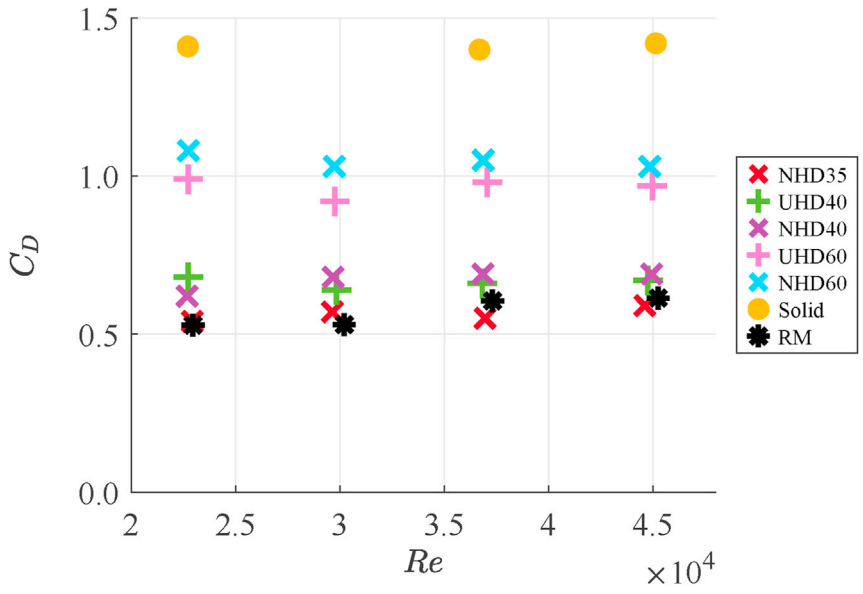

Fig. 3. The drag coefficient as a function of incoming Reynolds number for all turbine models.

Table 2
Average C_D for the RM and the disks with 35% and 40% solidity across measurements taken at different Reynolds numbers, and the associated standard deviation.

Disk type	Average C_D	C_D standard deviation
RM	0.57	0.08
NHD35	0.56	0.05
UHD40	0.66	0.05
NHD40	0.67	0.06

Based on the mean velocity field and drag results, the two lowest Reynolds number cases, $Re_D = 1.5 \times 10^4$ and $Re_D = 2.3 \times 10^4$, illustrate a dependence on the Reynolds number. To avoid Reynolds number effects in the following analysis, the rest of the PIV measurements were performed at the lowest Reynolds number within the Reynolds independent regime, $Re_D = 3 \times 10^4$, in order to limit other detrimental factors, e.g., the models auto-yawing inadvertently during a test; any test where this was observed was repeated such that none of the results presented herein represent yawed turbines.

5. Mean velocity fields

The velocity in the wake is the first characteristic used to compare the RM with the actuator disks. The time averaged total velocity $|\mathbf{U}|$ was normalized by the incoming velocity U_h, and is depicted in Fig. 5 for the RM and each actuator disk. The vectors indicate the magnitude and the direction. A mask has been applied over the model and to the area affected by shadows and laser reflection near the tower. The total velocity up to $1D$ upstream of the models is also included in Fig. 5.

The total velocity upstream of the actuator disks indicates that the incoming flow slows directly in front of the disks, and that the slowdown increases in magnitude and covers a larger area as the solidity of the disks increase. The slowdown in front of the blades of the RM has a smaller magnitude than what can be seen for the NHD35, showing that the RM imposes less of a blockage to the incoming flow. Although subtle, this result has implications for blockage estimates made for wind farms using either free RMs or actuator disks, which have been demonstrated to have

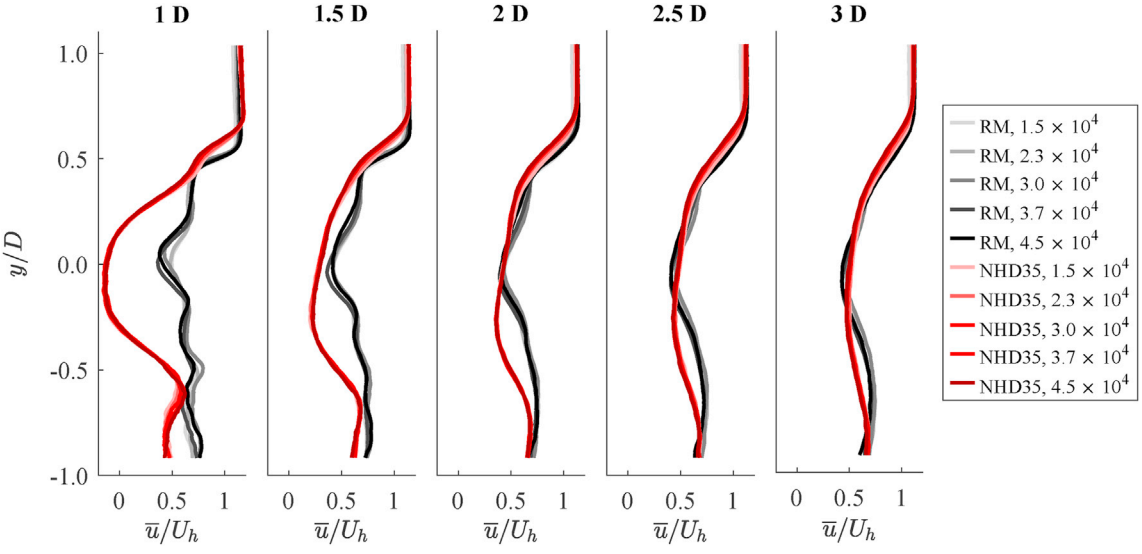

Fig. 4. Normalized u velocity downstream of the RM and the NHD35 actuator disk for different incoming Reynolds numbers.

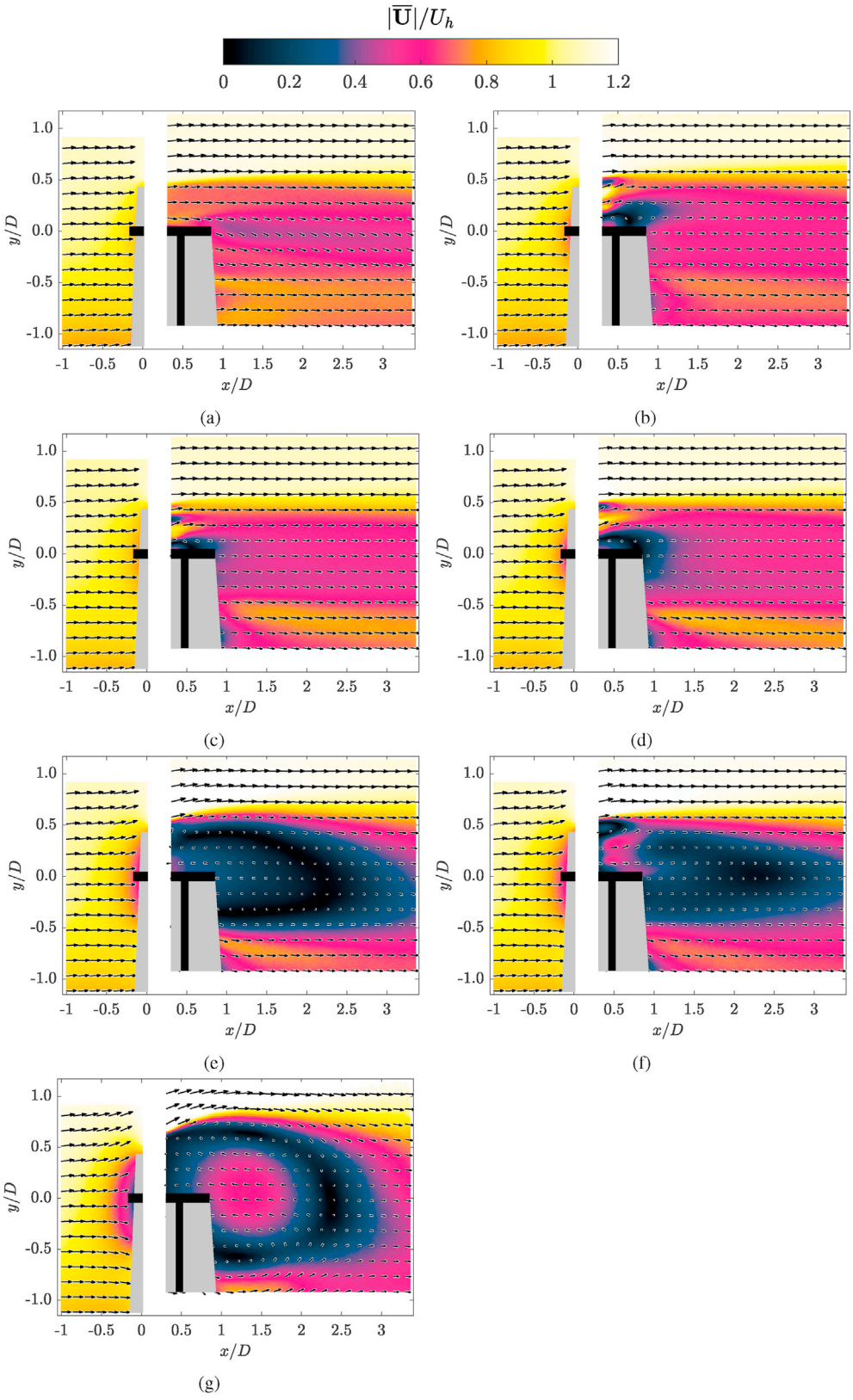

Fig. 5. Normalized total velocity fields for (a) the RM, (b) NHD35, (c) UHD40, (d) NHD40, (e) UHD60, (f) NHD60 and (g) the solid disk.

different blockage effects here.

The solid disk produces a significant recirculation area as a result of its large blockage. The UHD60 also induces a large area of reversed flow, and neither are thus comparable to the RM. The remaining actuator disks have a small recirculation area directly behind the disk, that is only present less than 1D downstream, and thus only affects the comparability of the disks and the RM in the immediate wake.

It is evident that the solid disk and the disks with 60% solidity have

considerable areas of deviation from the RM, which agrees with the drag measurements. Furthermore, the NHD40 deviates more from the RM than the UHD40 and NHD35. UHD40 and NHD35 both show good agreement with the RM, with the main difference being less than 1*D* downstream. The two have similar magnitude of deviation after 1*D*, however, the UHD40 is slightly closer to the RM when averaging the absolute value of the deviations.

Fig. 6 shows the normalized *u* velocity, being the dominant velocity component, at five different downstream locations as well as one upstream location. The tip vortices present at the upper edge of the RM's wake (distinctly visible in Fig. 1a and comparable to those found by Hong et al. (2014)) induce a steep velocity gradient seen at 1*D* downstream. The gradient then flattens as one moves farther downstream and the tip vortices lose strength. The actuator disks show a smoother transition between the freestream and the wake at 1*D* downstream. The velocity variations in the wake of the actuator disks homogenize quickly compared to the RM's wake. This is because the actuator disks transfer kinetic energy in the flow into turbulence which quite quickly decays (Batchelor and Townsend, 1947, 1948a,b). The actuator disks with low solidity have a high velocity gradient region in the same vertical position as the RM, however, this region of high velocity gradient occurs farther from the centre of the disk as the solidity of the disk increases. Overall, Fig. 6 indicates that the magnitude of *u* behind the RM is comparable to the magnitude of *u* generated by NHD35, NHD40 and UHD40 from 1.5*D* downstream.

6. Vorticity

In order to understand the organization of vortical structures in the wake of the RM and the actuator disks, the vorticity is examined. The time averaged out-of-plane vorticity ω_z was normalized using the incoming flow velocity U_h and the disk diameter D. Fig. 7 shows the normalized vorticity for each actuator disk and the RM. The solid disk and the disks with 60% solidity create two distinct areas of high magnitude vorticity, covering large parts of the wake, and thus differ from the lower solidity disks which seem to mainly produce vorticity at the upper and lower edges of the wake. This vorticity seen at the edges of the wake may be caused by vortices created at the disk edges or as a result of the interaction between the wake and the free-stream. Additional vorticity is present directly behind the actuator disks, which is likely caused by the turbulent flow through the holes in the disks, and the interaction of these flows behind the disks (Ertunç et al., 2010; Mazellier and Vassilicos, 2010).

The RM also produces high levels of vorticity along the upper and lower edges of the wake, as a result of tip vortices from the rotor blades. The upper line of vorticity is stronger and preserves its strength for a longer distance downstream than is the case with the low solidity actuator disks. However, towards the end of the field of view, this strong vortex sheet breaks down and the vorticity diffuses. There is also vorticity present in the center of the wake of the RM, possibly representing the root vortex from the hub (Lignarolo et al., 2016b).

A quantitative comparison was made to determine which of the disk

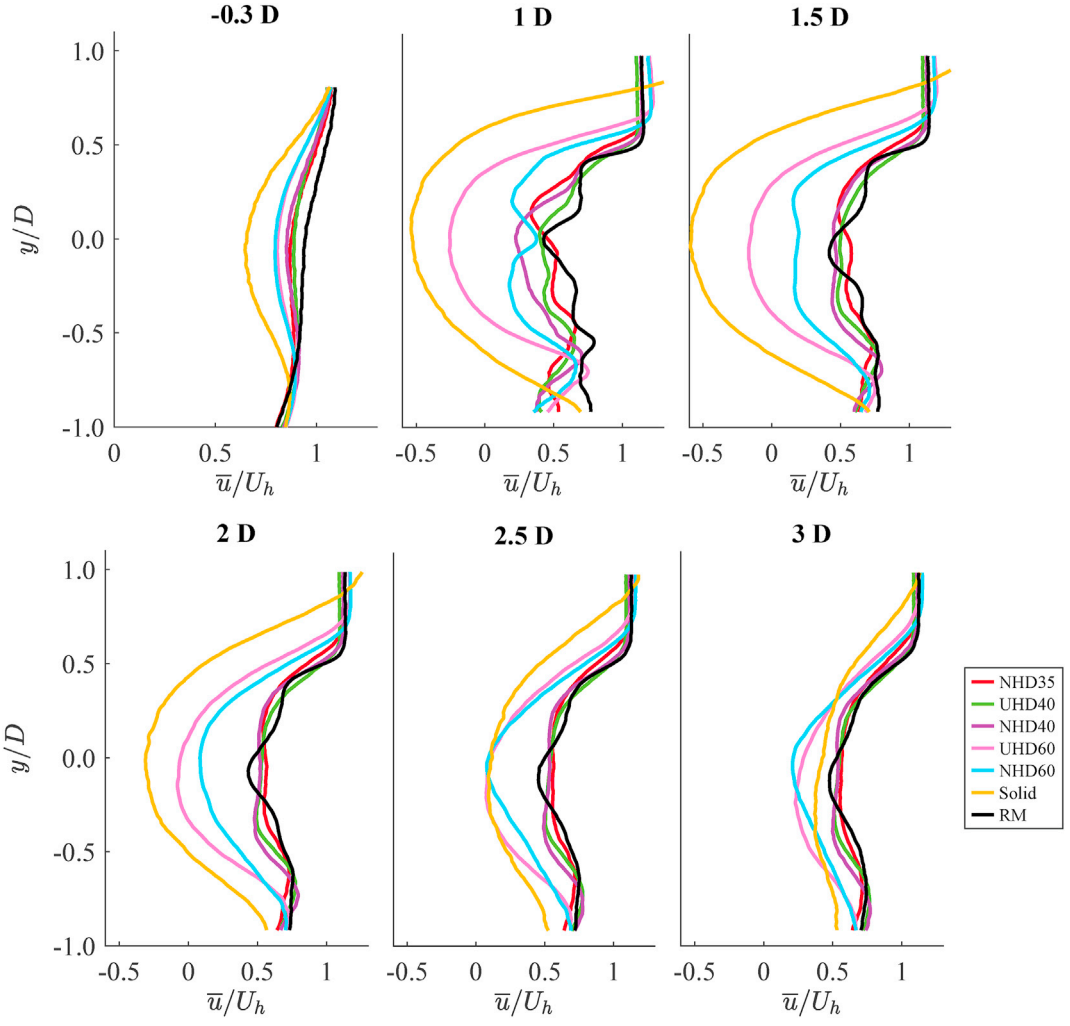

Fig. 6. Normalized *u* velocity at one upstream and five downstream locations for the RM and each actuator disk.

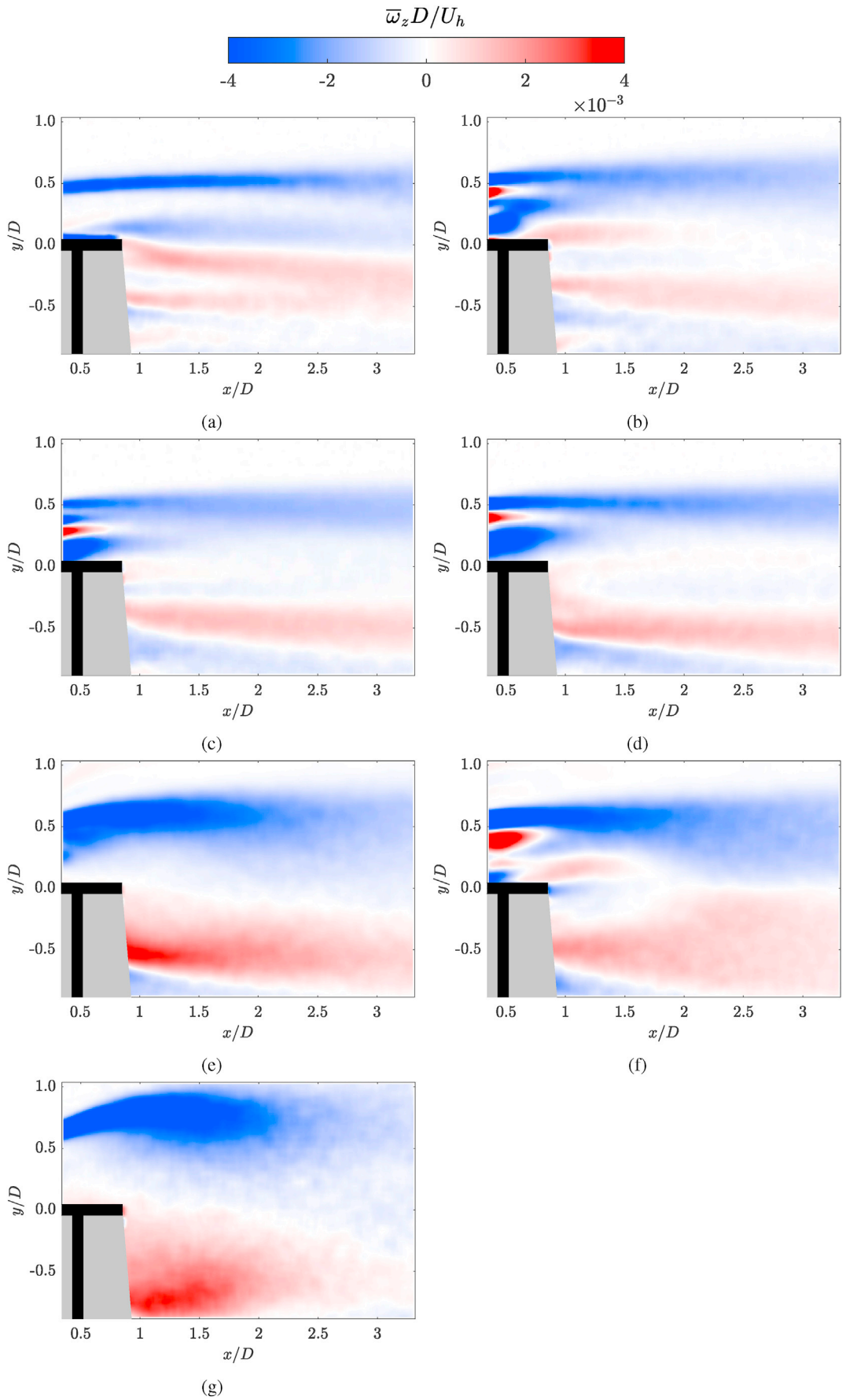

Fig. 7. Normalized vorticity fields for (a) the RM, (b) NHD35, (c) UHD40, (d) NHD40, (e) UHD60, (f) NHD60 and (g) the solid disk.

wakes has the vorticity field that best resembles the vorticity downstream of the RM. Close to the disks, the exact position of the holes is important for the vorticity field. To avoid these effects in the comparison, only the flow field downstream of 1.5D was evaluated. Two metrics have been used to evaluate which of the disks best resembles the RM. First, the magnitude of the average difference between the vorticity vectors of the RM and the disks have been calculated. The 40% and 35% solidity disks resemble the RM the most, with the NHD35 showing the smallest difference. Second, the percentage of vorticity vectors showing the same sign as the RM was counted. The number of vectors with the same sign is similar for most of the disks, with values around 80%. The results for both metrics are shown in Table 3. Using these metrics, the NHD35 is the closest match to the RM downstream of 1.5D.

Going forth, the analysis will be focused on only one actuator disk. Since NHD35 is the closest match in terms of the drag and the mean vorticity field, the remaining analysis will focus on this disk. For completeness, the results for the other disks are provided in the Supplementary Material to this work. The chosen disk is compared to the RM for several mean metrics, in a similar manner to previous actuator disk studies. However, in this case, in order to gain knowledge about the underlying mechanisms of the flow, more than just mean quantities are studied.

The mean vorticity field is a result of instantaneous swirl, and thus, the instantaneous swirl can provide information about the flow structures that cause vorticity in the flow. Swirling strength is defined as the second invariant of the velocity gradient tensor as described by Jeong and Hussain (1995). Fig. 8 shows an image of the instantaneous swirling strength, signed by vorticity, for the RM and the NHD35. These images are representative of the 1000 PIV measurements that were taken. The main difference between the two is the strong, distinct swirl seen at the upper edge of the wake for the RM, caused by tip vortices from the rotor blades. The actuator disk also has some swirl in the upper part of the wake, however it has a significantly lower strength than the distinct vortices from the RM, and it resembles the swirl at the lower edge of the wake and close to the wind tunnel floor. This swirl may be formed by the roll-up of the shear layer produced by the presence of the disk. The actuator disk also has high intensity swirl directly behind the disk, not seen after the RM's blades. As previously mentioned, this swirl is believed to be caused by the turbulent flow passing through the holes in the disk and the interaction of the jets behind the disk.

The important finding here is that even though averaging of the measurements resulted in similar sheets of vorticity at the upper edge of the wake, with an average local difference of less than 5% in the last half of the field of view, the instantaneous vortex structures differ. Many previous studies have used porous style disks which approximately match the drag and mean fields (Lignarolo et al., 2016b; Camp and Cal, 2016; Bossuyt et al., 2017). However, as indicated here when studying the instantaneous fields, the phenomenology in the flows might still be different.

7. Reynolds stresses

Another mean flow characteristic often examined when comparing actuator disks and RMs is the normal and shear Reynolds stresses. The normal Reynolds stresses are investigated here through the time averaged turbulence intensity, expressed as the normalized root of the mean 2D turbulent kinetic energy

$$\frac{\sqrt{k_{2D}}}{U_h} = \frac{\sqrt{\frac{1}{2}(\overline{u'u'} + \overline{v'v'})}}{U_h,} \tag{2}$$

where $\overline{u'u'}$ and $\overline{v'v'}$ are the normal Reynolds stresses in the streamwise and wall-normal directions, respectively. The time averaged turbulence intensity in the wake of the RM and the NHD35 can be seen in Fig. 9.

The RM shows high turbulence intensity at the upper edge of the wake, stemming from the tip vortices. Towards the end of the field of view, the tip vortices start to break down, and the turbulence diffuses. The turbulence intensity at the upper edge of the wake behind the actuator disk indicates that vortices emerging at the disk edge are present in close vicinity of the disk, for $x/D < 1$. However, this turbulent structure quickly diffuses. The actuator disk shows a high concentration of turbulence intensity directly behind the disk, which then slowly diffuses throughout the wake. This highly turbulent region is likely caused by the turbulent mixing of the jets and the small recirculation zone as observed in section 5, akin to grid turbulence (Ertunç et al., 2010). The most evident difference between the two wakes is in this region shortly behind the disk, less than 1D downstream. Downstream of 2D, the average difference between the two fields is 12%.

The mean in-plane Reynolds shear stress, $\overline{u'v'}$, normalized with the incoming velocity squared, is shown in Fig. 10a for the RM and Fig. 10b for NHD35. The shear stress $\overline{u'v'}$ physically represents the vertical flux of momentum, with negative values indicating downward flux and positive values indicating upward flux. Hence, it can be seen that for both models, the upper part of the wake is dominated by negative $\overline{u'v'}$ and the lower part is dominated by positive $\overline{u'v'}$.

Both the RM and NHD35 produce more intense shear stress in the shear layer of the wake, caused by flow entrainment and mixing. For the actuator disk, an increased intensity of shear stress is observed directly downstream of the disk, likely caused by the same phenomena that causes increased normal stresses in this area, i.e., the turbulent mixing of the flow passing through the holes in the disk. The largest difference between the two flow fields is found in this region, for $x/D < 1$. Fig. 11 illustrates the shear stress along three downstream cross-sections. As can be seen, the differences between the shear stress produced by the two models diminishes as one moves farther downstream, and the shear stress is largely of the same order of magnitude. Thus, the mean characteristic of Reynolds stresses is comparable between the static disk and the RM.

8. Proper orthogonal decomposition

As the swirl indicated that the instantaneous phenomena in the wakes differ between the RM and NHD35, the spatial modes that make up the wake were investigated to gain an understanding of the underlying spatial structures in the flows. In order to examine this, POD was applied. POD was first developed for fluid mechanics by Lumley (1967). Sirovich (1987) then developed the method of snapshot POD, where each instantaneous PIV measurement is considered to be a snapshot of the flow. The analysis conducted in this study followed the steps described by Meyer et al. (2007).

Snapshot POD is used to find the spatial modes of the flow. The mean velocity field is considered to be the zeroth mode. The analysis then focuses on the fluctuating parts of the velocity components. The method states that each snapshot can be expanded in a series of POD modes. Thus, if $\mathbf{u}^{*n}$ is a vector containing all the fluctuating u and v velocities in snapshot n, $[u'^{n_1} \ldots u'^{n_M} v'^{n_1} \ldots v'^{n_M}]^T$, where M is the number of positions in the snapshot,

$$\mathbf{u}^{*n} = \sum_{i=1}^{N} a_i^n \boldsymbol{\varphi}^i. \tag{3}$$

Table 3
Comparison of vorticity downstream of $x = 1.5D$.

Disk	$\frac{\lvert\overline{\omega_{\text{Disk}}} - \overline{\omega_{\text{RM}}}\rvert}{\max(\overline{\omega_{\text{RM}}})}$	$\frac{\overline{\omega_{\text{Disk}}}}{\overline{\omega_{\text{RM}}}} \geq 0$ [%]
NHD35	0.0519	81.9
NHD40	0.0616	72.0
UHD40	0.0556	81.2
NHD60	0.0745	81.5
UHD60	0.0920	82.4
Solid	0.1205	79.8

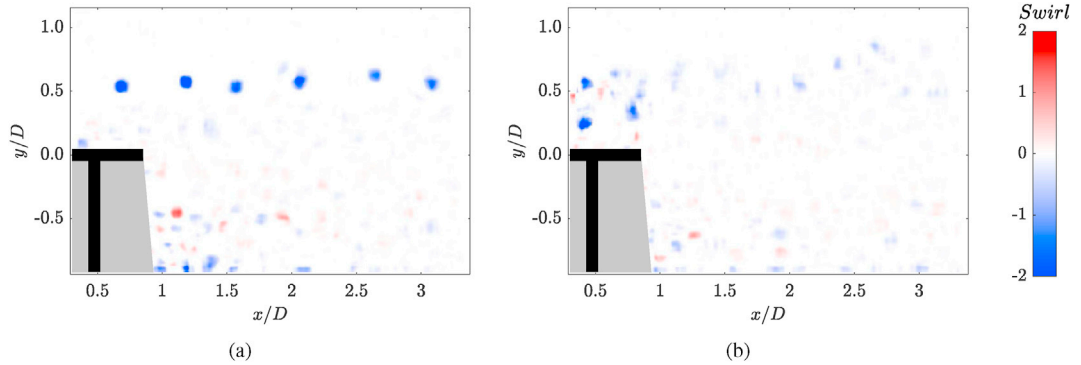

Fig. 8. Representative instantaneous swirling strength fields signed by vorticity for (a) the RM and (b) NHD35.

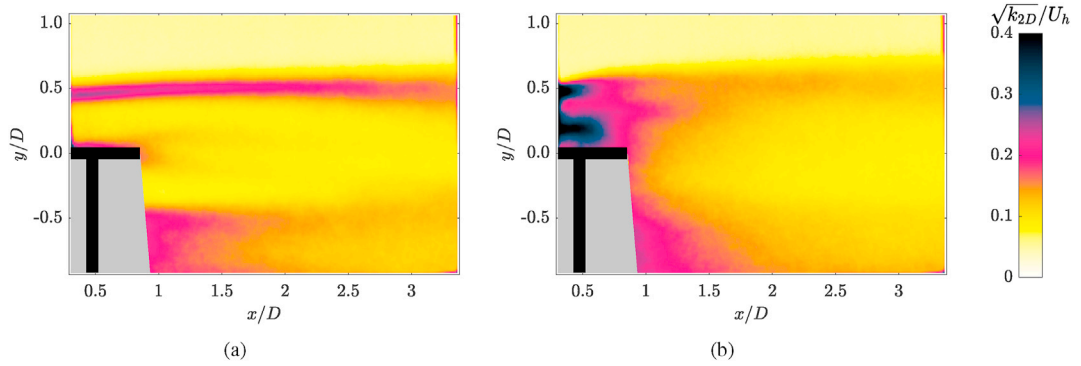

Fig. 9. Turbulence intensity fields for (a) the RM and (b) NHD35.

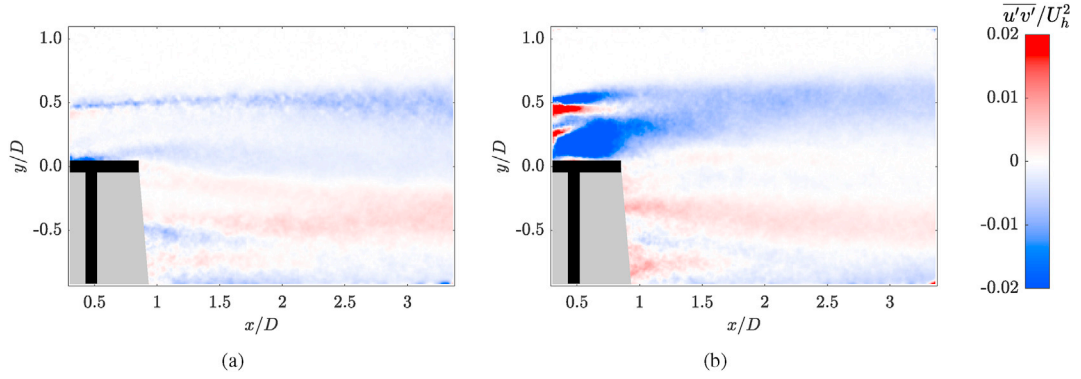

Fig. 10. Normalized Reynolds shear stress fields for (a) the RM and (b) NHD35.

Here, $\boldsymbol{\varphi}^i$ are the POD modes, and a_i^n are the POD coefficients related to snapshot n, determined by projecting the fluctuating part of the velocity field onto the POD modes. The analysis was performed on $N = 1000$ snapshots for each model.

The modes are ordered by their energy content, $[\lambda_1 \ldots \lambda_N]$, with lower numbered modes having higher energy content than higher numbered modes. Fig. 12 displays the cumulative energy of the modes for the RM and all the actuator disks. The NHD35 is the actuator disk which most closely resembles the RM in terms of the magnitude of energy contained in each mode. Additionally, both the RM and the NHD35 seem to have two particularly energetic modes.

Since 1000 vector fields have been used to construct the modes, 1000 modes would be required to capture all the energy in the velocity fluctuations. The number of modes required to capture a certain fraction of the energy can, however, provide some indication on the number of modes required to make a relevant approximation of the fluctuating velocity (van der Kindere and Ganapathisubramani, 2018). It is worth noting at this point that all the actuator disks and the RM require a relatively large number of modes to capture 50% of the energy in the flow, the RM requiring 129 modes and the NHD35 requiring 140 modes. This suggest that even though the few most energetic modes might provide information about the most energetic structures in each flow, the flows are not constructed of a few large, energetic structures. Rather, they seem to be complex flows with large amounts of local fluctuations, requiring many modes to be described.

When high-energy modes are present, these usually represent periodic, large-scale flow structures. However, the amount of energy contained in the modes does not imply anything about the shapes of the modes. Figs. 13 and 14 show the first mode of the fluctuating streamwise (φ_u^1) and vertical (φ_v^1) velocity components, respectively, for the RM and the NHD35. When examining the modes, the absolute values are insignificant, as each mode is coupled with a relative POD coefficient when

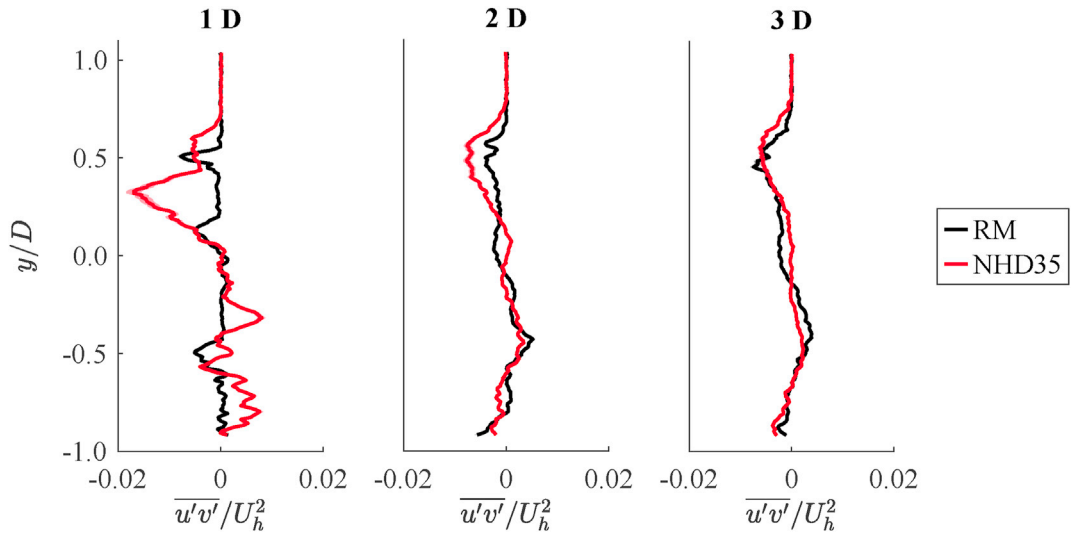

Fig. 11. Normalized Reynolds shear stress $\overline{u'v'}$ at three locations downstream of the RM and the NHD35.

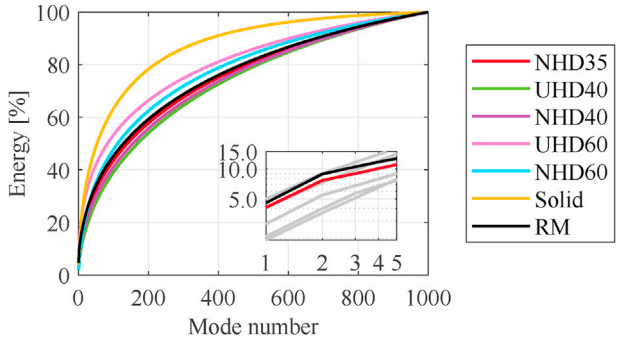

Fig. 12. Cumulative energy of the modes for all actuator disks and the RM. The inset is zoomed in on the five most energetic modes on log-log axes, with RM and NHD35 highlighted.

used to reconstruct the fluctuating velocities in a snapshot. The important factor is the relative values, demonstrating the length scale and location of the velocity fluctuations that contain a certain fraction of the total energy.

The first mode of the RM shows high intensity turbulent kinetic energy at the upper and lower edges of the wake, which seem to represent the kinetic energy in the tip vortices from the blades. These energetic structures start right behind the rotor blades and are still visible at the end of the field of view, but do, however, seem to decrease in intensity farther downstream. As previously mentioned, Camp and Cal (2019) studied the POD modes of actuator disks and RMs in the *xy*-plane. They found a prominent feature near the top tip of the wake in φ_u^1. However, the tip vortices found behind the RM in Fig. 13 are more distinct. Additionally, tip vortices can be observed in φ_v^1 in this case.

The first mode in the wake of NHD35 also demonstrates repeating structures, suggesting a periodic shedding structure is also present for this disk, but with very different dynamics to that in the wake of the RM. There is high intensity turbulent kinetic energy directly behind the disk, suggesting high velocity fluctuations at this location. These fluctuations might be connected to the turbulent mixing of the flow jets passing through the holes in the disk.

Comparing the modes of the RM and the NHD35, it is evident that the most energetic structures in the two flows are fundamentally different. The energetic structures in the modes of the RM are concentrated around the edges of the wake, whereas for NHD35, the energetic structures are to a larger extent present in the center of the wake. A difference can also be seen in terms of the length scale of the structures. The RM indicates small

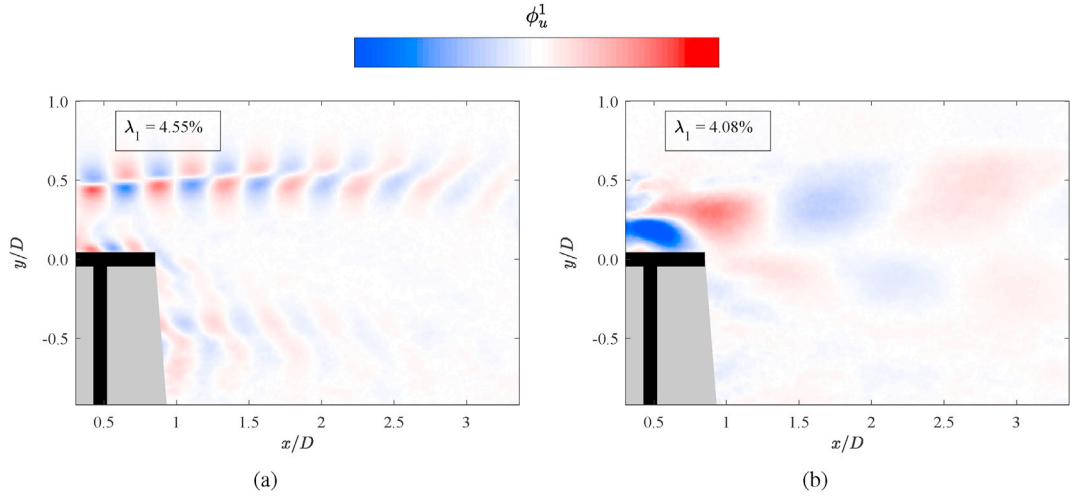

Fig. 13. φ_u^1 for (a) the RM and (b) NHD35. Only the relative values are of importance. λ_1 expresses the percentage of the total fluctuating energy found in the first velocity mode.

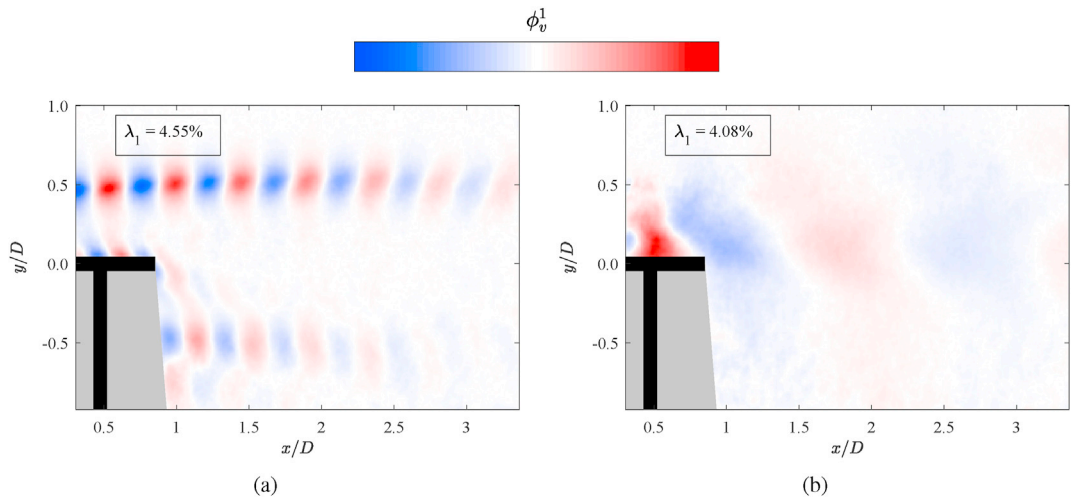

Fig. 14. φ_v^1 for (a) the RM and (b) NHD35. Only the relative values are of importance. λ_1 expresses the percentage of the total fluctuating energy found in the first velocity mode.

energetic structures, with the velocity fluctuations quickly changing direction. The actuator disk illustrates significantly larger, and thus fewer, structures. As previously seen in terms of the instantaneous swirling strength, the tip vortices stemming from the RM are evident, and such strong tip vortices do not appear in the case of the actuator disk. None of the actuator disks showed similar behavior to the RM when studying their modes.

9. Conclusion

The near wake of a lab-scale rotating wind turbine model and multiple actuator disks of the same dimensions were studied experimentally in a wind tunnel with PIV. Actuator disks of two different designs and multiple different solidities were used in order to represent the different designs that have been employed by the existing literature. Both designs, as well as the RM, are representative of lab-scale wind turbine models found in the literature. The process of actuator disk selection, which is often implicit in actuator disk research, is explicitly shown by presenting the results from drag measurements as well as the mean velocity and vorticity fields in the wake.

The normalized total velocity in the wake of the RM and each actuator disk was compared, showing that the high solidity disks had too large blockage, which led to a significant velocity deficit in the wake. The velocity field that developed behind the low solidity disks agreed well with the wake of the RM. Nonetheless, all actuator disks showed a recirculation region that was limited to $x/D < 1$ for the lower solidity disks.

The out-of-plane vorticity in the wakes was subsequently compared. The RM showed increased intensity of vorticity along the upper edge of the wake, induced by tip vortices. The actuator disks also showed increased levels of vorticity along the edges of the wake. The lower solidity disks showed high intensity vorticity directly behind the disks, induced by turbulent mixing of the flow jets passing through the holes of the disks.

The NHD35 actuator disk was the closest match to the RM in terms of drag coefficient and mean wake vorticity, and was thus studied in further detail. In previous studies, the comparison has been limited to mean characteristics. Since the mean vorticity field is a result of instantaneous swirl, the instantaneous swirling strength signed by vorticity was studied in the present work. It illustrated that instantaneous tip vortices were present behind the RM, but not behind the NHD35. Additionally, high intensity swirl was seen directly behind the actuator disk, which again was believed to be related to the mixing of the flow jets through the disk holes.

The normal and shear Reynolds stresses of the NHD35 and the RM were comparable. The difference between the two wakes was limited to the area $x/D < 1$.

POD analysis was conducted to analyze the underlying instantaneous phenomena of the two flows. It showed how the most energetic mode for the RM represented the upper and lower tip vortices, which were not present for the actuator disk. The energetic velocity fluctuations differed both in terms of length scale and location. This implies that the main structures constituting the two flows are different.

Despite having fairly good agreement between the RM and the actuator disk across many mean parameters, including drag, velocity, vorticity and Reynolds shear stress, the modal structure of the flows were still different. The underlying, instantaneous flow phenomena in the near wake of the actuator disk are thus not representative of a RM.

Actuator disks are clearly good for capturing mean flow properties, but as this study has shown, instantaneous phenomena in the wake are not always well captured. Moreover, the upstream blockage effect of the actuator disks and RMs differed. Therefore, as actuator disks will continue to be used, it is important to understand all aspects of their flow behavior. This will contribute to a better understanding in studies in which they are employed, and may also help in the development of different disk designs which better capture higher order and instantaneous flow features.

CRediT authorship contribution statement

Sanne de Jong Helvig: Methodology, Software, Validation, Formal analysis, Investigation, Writing - original draft, Visualization. **Magnus K. Vinnes:** Conceptualization, Methodology, Software, Validation, Investigation, Writing - review & editing. **Antonio Segalini:** Resources, Writing - review & editing. **Nicholas A. Worth:** Conceptualization, Resources, Writing - review & editing, Supervision, Project administration. **R. Jason Hearst:** Conceptualization, Resources, Writing - review & editing, Supervision, Project administration.

Declaration of competing interest

The authors declare that they have no known competing financial interests or personal relationships that could have appeared to influence the work reported in this paper.

Acknowledgements

The authors would like to acknowledge the support of M. Asadi who

participated in and supported the PIV measurement campaign.

Appendix A. Supplementary data

Supplementary data to this article can be found online at https://doi.org/10.1016/j.jweia.2020.104485.

References

Aubrun, S., Bastankhah, M., Cal, R., Conan, B., Hearst, R., Hoek, D., Hölling, M., Huang, M., Hur, C., Karlsen, B., Neunaber, I., Obligado, M., Peinke, J., Percin, M., Saetran, L., Schito, P., Schliffke, B., Sims-Williams, D., Uzol, O., Vinnes, M., Zasso, A., 2019. Round-robin tests of porous disc models. J. Phys. Conf. 1256, 012004 https://doi.org/10.1088/1742-6596/1256/1/012004.

Aubrun, S., Loyer, S., Hancock, P., Hayden, P., 2013. Wind turbine wake properties: comparison between a non-rotating simplified wind turbine model and a rotating model. J. Wind Eng. Ind. Aerod. 120, 1–8. https://doi.org/10.1016/j.jweia.2013.06.007.

Barthelmie, R.J., Churchfield, M.J., Moriarty, P.J., Lundquist, J.K., Oxley, G.S., Hahn, S., Pryor, S.C., 2015. The role of atmospheric stability/turbulence on wakes at the Egmond aan Zee offshore wind farm. J. Phys. Conf. 625 https://doi.org/10.1088/1742-6596/625/1/012002.

Barthelmie, R.J., Jensen, L.E., 2010. Evaluation of wind farm efficiency and wind turbine wakes at the Nysted offshore wind farm. Wind Energy 13. https://doi.org/10.1002/we.408.

Batchelor, G., Townsend, A., 1947. Decay of vorticity in isotropic turbulence. Proc. Math. Phys. Eng. Sci. 190, 534–550. https://doi.org/10.1098/rspa.1947.0095.

Batchelor, G.K., Townsend, A.A., 1948a. Decay of isotropic turbulence in the initial period. Proc. Roy. Soc. Lond. Math. Phys. Sci. 193, 539–558. http://www.jstor.org/stable/98061.

Batchelor, G.K., Townsend, A.A., 1948b. Decay of turbulence in the final period. Proc. Roy. Soc. Lond. Math. Phys. Sci. 194, 527–543. http://www.jstor.org/stable/98265.

Blackmore, T., Batten, W., Muller, G., Bahaj, A., 2013. Influence of turbulence on the drag of solid discs and turbine simulators in a water current. Exp. Fluid 55. https://doi.org/10.1007/s00348-013-1637-9.

Bossuyt, J., Howland, M., Meneveau, C., Meyers, J., 2017. Measurement of unsteady loading and power output variability in a micro wind farm model in a wind tunnel. Exp. Fluid 58. https://doi.org/10.1007/s00348-016-2278-6.

Camp, E., Cal, R., 2016. Mean kinetic energy transport and event classification in a model wind turbine array versus an array of porous disks: energy budget and octant analysis. Phys. Rev. Fluid. 1, 044404 https://doi.org/10.1103/PhysRevFluids.1.044404.

Camp, E., Cal, R., 2019. Low-dimensional representations and anisotropy of model rotor versus porous disk wind turbine arrays. Phys. Rev. Fluid. 4 https://doi.org/10.1103/PhysRevFluids.4.024610.

Cardesa, J.I., Nickels, T.B., Dawson, J.R., 2012. 2D PIV measurements in the near field of grid turbulence using stitched fields from multiple cameras. Exp. Fluid 52, 1611–1627.

Ebenhoch, R., Muro, B., Dahlberg, J.Å., Berkesten Hägglund, P., Segalini, A., 2017. A linearized numerical model of wind-farm flows. Wind Energy 20, 859–875. https://doi.org/10.1002/we.2067.

Ertunç, O., Ozyilmaz, N., Lienhart, H., Durst, F., 2010. Homogeneity of turbulence generated by static-grid structures. J. Fluid Mech. 654, 473–500. https://doi.org/10.1017/S0022112010000479.

Harrison, M., Batten, W., Myers, L., Bahaj, A., 2010. Comparison between CFD simulations and experiments for predicting the far wake of horizontal axis tidal turbines. Renew. Power Generat. IET 4, 613–627. https://doi.org/10.1049/iet-rpg.2009.0193.

Hearst, R.J., Ganapathisubramani, B., 2017. Tailoring incoming shear and turbulence profiles for lab-scale wind turbines. Wind Energy 20, 2021–2035. https://doi.org/10.1002/we.2138.

Hong, J., Toloui, M., Chamorro, L., Guala, M., Howard, K., Riley, S., Tucker, J., Sotiropoulos, F., 2014. Natural snowfall reveals large-scale flow structures in the wake of a 2.5-MW wind turbine. Nat. Commun. 5, 4216. https://doi.org/10.1038/ncomms5216.

Howland, M.F., Bossuyt, J., Martínez-Tossas, L.A., Meyers, J., Meneveau, C., 2016. Wake structure in actuator disk models of wind turbines in yaw under uniform inflow conditions. J. Renew. Sustain. Energy 8. https://doi.org/10.1063/1.4955091.

Jeong, J., Hussain, F., 1995. On the identification of a vortex. J. Fluid Mech. 285, 69–94. https://doi.org/10.1017/S0022112095000462.

Li, L., Hearst, R.J., Ferreira, M.A., Ganapathisubramani, B., 2020. The near-field of a lab-scale wind turbine in tailored turbulent shear flows. Renew. Energy 149, 735–748. https://doi.org/10.1016/j.renene.2019.12.049.

Lignarolo, L., Mehta, D., Stevens, R., Yilmaz, A., Kuik, G., Andersen, S., Meneveau, C., Ferreira, C., Ragni, D., Meyers, J., van Bussel, G., Holierhoek, J., 2016a. Validation of four LES and a vortex model against stereo-PIV measurements in the near wake of an actuator disc and a wind turbine. Renew. Energy 94, 510–523. https://doi.org/10.1016/j.renene.2016.03.070.

Lignarolo, L., Ragni, D., Ferreira, C., van Bussel, G., 2014. Kinetic energy entrainment in wind turbine and actuator disc wakes: an experimental analysis. J. Phys. Conf. 524, 012163 https://doi.org/10.1088/1742-6596/524/1/012163.

Lignarolo, L., Ragni, D., Ferreira, C., van Bussel, G., 2016b. Experimental comparison of a wind-turbine and of an actuator-disc near wake. J. Renew. Sustain. Energy 8, 023301. https://doi.org/10.1063/1.4941926.

Lumley, J.L., 1967. The Structure of Inhomogeneous Turbulent Flows.

Martínez Tossas, L., Churchfield, M., Leonardi, S., 2014. Large eddy simulations of the flow past wind turbines: actuator line and disk modeling. Wind Energy 18. https://doi.org/10.1002/we.1747.

Mazellier, N., Vassilicos, J.C., 2010. Turbulence without Richardson–Kolmogorov Cascade. Physics of Fluids 22. https://doi.org/10.1063/1.3453708.

Meyer, K.E., Pedersen, J.M., Özcan, O., 2007. A turbulent jet in crossflow analysed with proper orthogonal decomposition. J. Fluid Mech. 583, 199–227. https://doi.org/10.1017/S0022112007006143.

Myers, L., Bahaj, A., 2010. Experimental analysis of the flow field around horizontal axis tidal turbines by use of scale mesh disk rotor simulators. Ocean. Eng. 37, 218–227. https://doi.org/10.1016/j.oceaneng.2009.11.004.

Neal, D.R., Sciacchitano, A., Smith, B.L., Scarano, F., 2015. Collaborative framework for PIV uncertainty quantification: the experimental database. Meas. Sci. Technol. 26, 074003.

Neunaber, I., 2018. Stochastic investigation of the evolutoon of small-scale turbulence in the wake of a wind turbine exposed to different inflow conditions. Ph.D. thesis. Carl von Ossietzky Universität Oldenburg.

Pierella, F., Sætran, L., 2010. Effect of initial conditions on flow past grids of finite extension. In: 17th Australasian Fluid Mechanics Conference 2010.

Porté-Agel, F., Bastankhah, M., Shamsoddin, S., 2019. Wind-turbine and wind-farm flows: a review. Boundary-Layer Meteorol. https://doi.org/10.1007/s10546-019-00473-0.

Sciacchitano, A., Neal, D.R., Smith, B.L., Warner, S.O., Vlachos, P.P., Wieneke, B., Scarano, F., 2015. Collaborative framework for PIV uncertainty quantification: comparative assessment methods. Meas. Sci. Technol. 26, 074004.

Segalini, A., Dahlberg, J.Å., 2020. Blockage effects in wind farms. Wind Energy 23, 120–128. https://doi.org/10.1002/we.2413.

Sforza, P., Sheerin, P., Smorto, M., 1981. Three-dimensional wakes of simulated wind turbines. AIAA J. 19, 1101–1107. https://doi.org/10.2514/3.60049.

Siemens, 2019. The socioeconomic impacts of wind energy in the context of the energy transition. https://www.siemensgamesa.com/explore/journal/socioeconomic-report-wind-energy-2019. Online; accessed 12-December-2019.

Simisiroglou, N., Breton, S., Ivanell, S., 2017. Validation of the actuator disc approach using small-scale model wind turbines. Wind Energy Sci. 2, 587–601. https://doi.org/10.5194/wes-2-587-2017.

Sirovich, L., 1987. Turbulence and the dynamics of coherent structures. i - coherent structures. ii - symmetries and transformations. iii - dynamics and scaling. Q. Appl. Math. 45 https://doi.org/10.1090/qam/910463.

Skeide, A.K., Bardal, L.M., Oggiano, L., Hearst, R.J., 2020. The significant impact of ribs and small-scale roughness on cylinder drag crisis. J. Wind Eng. Ind. Aerod. 202 https://doi.org/10.1016/j.jweia.2020.104192.

Smith, C., Barthelmie, R., Pryor, S., 2013. In situ observations of the influence of large onshore wind farm on near-surface temperature, turbulence intensity, and wind speed profiles. Environ. Res. Lett. 8 https://doi.org/10.1088/1748-9326/8/3/034006.

Stevens, R.J.A.M., Gayme, D., Meneveau, C., 2014. Large eddy simulation studies of the effects of alignment and wind farm length. J. Renew. Sustain. Energy 6. https://doi.org/10.1063/1.4869568.

Stevens, R.J.A.M., Meneveau, C., 2014. Temporal structure of aggregate power fluctuations in large-eddy simulations of extended wind-farms. J. Renew. Sustain. Energy 6. https://doi.org/10.1063/1.4885114.

Stevens, R.J.A.M., Meneveau, C., 2017. Flow structure and turbulence in wind farms. Annu. Rev. Fluid Mech. 49 https://doi.org/10.1146/annurev-fluid-010816-060206.

Sunada, S., Sakaguchi, A., Kawachi, K., 1997. Airfoil section characteristics at a low Reynolds number. J. Fluid Eng. 119, 129–135. https://doi.org/10.1115/1.2819098.

Theunissen, R., Housley, P., Allen, C., Carey, C., 2015. Experimental verification of computational predictions in power generation variation with layout of offshore wind farms. Wind Energy 18. https://doi.org/10.1002/we.1788.

Theunissen, R., Worboys, R., 2018. Near-wake observations behind azimuthally perforated disks with varying hole layout and porosity in smooth airstreams at high Reynolds numbers. J. Fluid Eng. 141 https://doi.org/10.1115/1.4041614.

van der Kindere, J., Ganapathisubramani, B., 2018. Effect of length of two-dimensional obstacles on characteristics of separation and reattachment. J. Wind Eng. Ind. Aerod. 178, 38–48. https://doi.org/10.1016/j.jweia.2018.04.018.

Veers, P., Dykes, K., Lantz, E., Barth, S., Bottasso, C., Carlson, O., Clifton, A., Green, J., Green, P., Holttinen, H., Laird, D., Lehtomäki, V., Lundquist, J., Manwell, J., Marquis, M., Meneveau, C., Moriarty, P., Munduate, X., Muskulus, M., Wiser, R., 2019. Grand challenges in the science of wind energy. Science eaau2027. https://doi.org/10.1126/science.aau2027.

Wieneke, B., 2015. PIV uncertainty quantification from correlation statistics. Meas. Sci. Technol. 26, 074002.

Wu, Y., Porté-Agel, F., 2011. Large-eddy simulation of wind-turbine wakes: evaluation of turbine parametrisations. Boundary-Layer Meteorol. 138 https://doi.org/10.1007/s10546-010-9569-x.

Wu, Y., Porté-Agel, F., 2012. Atmospheric turbulence effects on wind-turbine wakes: an LES study. Energies 5, 5340–5362. https://doi.org/10.3390/en5125340.

Zhan, L., Letizia, S., Iungo, G., 2019. LiDAR measurements for an onshore wind farm: wake variability for different incoming wind speeds and atmospheric stability regimes. Wind Energy. https://doi.org/10.1002/we.2430.

Zhan, L., Letizia, S., Iungo, G., 2020. Wind LiDAR measurements of wind turbine wakes evolving over flat and complex terrains: ensemble statistics of the velocity field. J. Phys. Conf. 1452 https://doi.org/10.1088/1742-6596/1452/1/012077.